Retrieval of Solar-induced Chlorophyll Fluorescence from Satellite Measurements: Comparison of SIF between TanSat and OCO-2

Lu Yao[1,2], Yi Liu[1,3], Dongxu Yang[1,3], Zhaonan Cai[1], Jing Wang[1], Chao Lin[4], Naimeng Lu[5], Daren Lyu[1], Longfei Tian[6], Maohua Wang[3], Zengshan Yin[6], Yuquan Zheng[4], Sisi Wang[7]

[1]Key Laboratory of Middle Atmosphere and Global Environment Observation, Institute of Atmospheric Physics, Chinese Academy of Sciences, No. 40, Huayan Li, Chaoyang District, Beijing 100029, China
[2]University of Chinese Academy of Sciences, No. 19A, Yuquan Lu, Shijing Shan District, Beijing 100049, China
[3]Shanghai Advanced Research Institute, Chinese Academy of Sciences, Shanghai 201210, China
[4]Changchun Institute of Optics, Fine Mechanics and Physics, Changchun 130033, China
[5]National Satellite Meteorological Center, China Meteorological Administration, Beijing 100081, China
[6]Shanghai Engineering Center for Microsatellites, Shanghai 201203, China
[7]National Remote Sensing Center of China, Beijing 100036, China

Correspondence to: Dongxu Yang (yangdx@mail.iap.ac.cn)

Abstract. Solar-induced chlorophyll fluorescence (SIF) is emitted during photosynthesis in plant leaves. It constitutes a small additional offset to reflected radiance and can be observed by sensitive instruments that with high signal-to-noise ratio and spectral resolution. The Chinese global carbon dioxide monitoring satellite (TanSat), as its mission, acquires greenhouse gas column density. The advanced technical characteristics of the hyper-spectrum grating spectrometer (ACGS) onboard TanSat enable SIF retrieval from space observations in the O_2-A band. In this study, one-year SIF data for each sounding was retrieved from Orbiting Carbon Observatory-2 (OCO-2) and TanSat measurements using the IAPCAS/SIF algorithm. A comparison between the SIF results retrieved from OCO-2 spectra and the official OCO-2 SIF product (OCO2_Level 2_Lite_SIF.8r) shows their strong linear relationship ($R^2 > 0.85$) and suggests the reliability of the SIF retrieval algorithm. The global distribution showed that the SIF retrieved from the two satellites shared the same spatial pattern for all seasons with the gridded SIF difference less than 0.3 W m^{-2} μm^{-1} sr^{-1}, and they also agreed well with the official OCO-2 SIF product with the difference less than 0.2 W m^{-2} μm^{-1} sr^{-1}. The retrieval uncertainty of seasonal-gridded TanSat SIF is less than 0.03 W m^{-2} μm^{-1} sr^{-1} whereas the uncertainty of each sounding ranges from 0.1 to 0.6 W m^{-2} μm^{-1} sr^{-1}. The relationship between annually-averaged SIF products and FLUXCOM gross primary productivity (GPP) was also estimated for six vegetation types in a 1° × 1° grid over the globe, indicating that the SIF data from the two satellites have the same potential in quantitatively characterizing ecosystem productivity. The spatiotemporal consistency between TanSat and OCO-2 and their comparable data quality make the comprehensive usage of the two mission products possible. Data supplemented by TanSat observations are expected to contribute to the development of global SIF maps with more spatiotemporal detail, which will advance global research on vegetation photosynthesis.

1 Introduction

Terrestrial vegetation accounts for a large part of the ecosystem, with its photosynthesis and respiration processes playing important roles in the global carbon cycle. Incoming radiation is absorbed, reflected, and/or transmitted by plant leaves. A portion of the absorbed radiation is used by the chlorophyll in plant leaves for carbon fixation, while the rest is either dissipated as heat or re-emitted as solar-induced chlorophyll fluorescence (SIF) at longer wavelengths (Frankenberg et al., 2011a, 2014). In contrast to the traditional remotely sensed vegetation indices obtained from some studies (Frankenberg et al., 2011b; Guanter et al., 2014; Li et al., 2018; Sun et al., 2017a; Yang et al., 2015; Zhang et al., 2014), SIF offers the potential to measure photosynthesis activity and gross primary production (GPP), due to the strong correlation between these measures (Frankenberg et al., 2011b; Guanter et al., 2012, 2014). The fluorescence emission (Fs) adds a low-intensity radiance less than 10 W m^{-2} μm^{-1} sr^{-1} and fills in the solar absorption features of the reflected spectrum (Frankenberg et al., 2011a). The filling-in effect of the solar lines (Fraunhofer lines) is the basic principle applied to measure SIF from space using the capabilities of hyperspectral observation (Frankenberg et al., 2011b; Guanter et al., 2012).

The first attempt at SIF research based on space-based observations was performed using images acquired by the Medium Resolution Imaging Spectrometer (MERIS) onboard the ENVIronmental SATellite (ENVISAT) (Guanter et al., 2007). This led to a new idea for conducting SIF studies on a global scale. The first global SIF map was retrieved with high-resolution spectra from the Greenhouse-gases Observing SATellite (GOSAT) (Joiner et al., 2011; Frankenberg et al., 2011b). After that, SIF retrievals were implemented from a variety of satellite measurements, such as those from the Global Ozone Monitoring Experiment-2 (GOME-2) instruments onboard meteorological operational satellites, SCIAMACHY on board ENVISAT, and Orbiting Carbon Observatory-2 (OCO-2) (Joiner et al., 2016; Köhler et al., 2015). The TROPOspheric Monitoring Instrument (TROPOMI) on board Sentinel 5 Precursor (S-5P) provides more efficient SIF observations in terms of global coverage and new opportunities for exploring the application potential of SIF data in the terrestrial biosphere as well as in climate research (Doughty et al., 2019; Köhler et al., 2018b). Furthermore, an upcoming European Space Agency mission called FLuorescence EXplorer (FLEX), the first satellite dedicated to SIF emission observation, will launch in the middle of 2024 (Drusch et al., 2017). Many studies on SIF applications have been initiated with the accumulation of SIF products in recent years. The responses of satellite-measured SIF to environmental conditions have been applied to drought dynamics monitoring and regional vegetation water stress estimation (Lee et al., 2013; Sun et al., 2015; Yoshida et al., 2015). As a proxy of photosynthesis, SIF acts as a powerful constraint parameter in estimating carbon exchange in an ecosystem between the atmosphere, ocean, and soil; as such, the analysis of the relationship between SIF and GPP has become an important research topic (Li et al., 2018; Köhler et al., 2018a; Sun et al., 2017a; Zhang et al., 2018). The strong linear relationship between them paves the way for improving terrestrial ecosystem model simulation of GPP, along with consequent improvement of global carbon flux estimation (MacBean et al., 2018; Yin et al., 2020). GPP estimations based on satellite-measured SIF have proven to be an effective method validated by in-situ flux observations (Joiner et al., 2018; Qiu et al., 2020). However, uncertainty in the factors that determine the relationship between SIF and GPP still exists and is a key

limitation in the application of SIF to flux estimation. Based on multi-satellite SIF products, eddy covariance flux tower observations, and ecological models, the relationship between SIF and GPP under different environmental conditions has been discussed in a number of studies to analyze the dominant factors for the growing status of different biomes, such as temperature, soil moisture, and vegetation types (Chen et al., 2020; Doughty et al., 2019; Li et al., 2020; Qiu et al., 2020; Yin et al., 2020).

The Chinese global carbon dioxide monitoring satellite (TanSat) was launched in December 2016. Aiming at acquiring CO_2 concentrations as OCO-2, TanSat flies in a sun-synchronous orbit at approximately 700 km in height with a 16-day repeat cycle and an equator crossing time of ~1:30 p.m. local time (Cai et al., 2014; Liu et al., 2018; Yang et al., 2018). Onboard TanSat, the hyperspectral Atmospheric Carbon-dioxide Grating Spectrometer (ACGS) is designed to separately record solar backscatter spectra in three channels centered at 0.76 μm (O_2-A band), 1.61 μm (weak CO_2 absorption band), and 2.06 μm (strong CO_2 absorption band). With the recorded spectra, many Optimal Estimation Method (OEM) full physics retrieval algorithms have been developed and applied for XCO_2 retrievals (Boesche et al., 2009; Butz et al., 2009, 2011; O'Dell et al., 2012; Reuter et al., 2010; Yang et al., 2015b; Yoshida et al., 2011, 2013). The Institute of Atmospheric Physics Carbon Dioxide Retrieval Algorithm for Satellite Remote Sensing (IAPCAS) algorithm has been applied for TanSat retrieval (Yang et al., 2018; Yang et al., 2021) and was also previously tested on GOSAT and OCO-2 missions (Yang et al., 2015b). However, the fluorescence feature causes substantial biases when retrieving surface pressure and scattering parameters from the O_2-A band, and the associated errors propagate into the XCO_2 retrievals. In previous XCO_2 retrieval, the surface emissions were well modeled as a continuum zero offset of the O_2-A band to reduce errors (Frankenberg et al., 2011a, 2012; Butz et al., 2009, 2010; Joiner et al., 2012). The high spectral resolution of ~0.044 nm and a signal-to-noise ratio of ~360 in the O_2-A band makes it possible to obtain SIF from space measurements, with a spatial resolution of 2 km × 2 km in nadir mode (Liu et al., 2018).

Various approaches have been used to infer SIF from satellite measurements (Frankenberg et al., 2011b, 2014a, 2014b; Guanter et al., 2007, 2012, 2015; Joiner et al., 2011, 2013, 2016; Köhler et al., 2015, 2018b). The SIF signal induces a filling-in effect of solar lines, which can be used for SIF retrieval, as the fractional depth of solar Fraunhofer lines does not change during radiation transmission in the atmosphere. To recognize the filling-in features by SIF, high-resolution spectra and an instrument spectral response function (ISRF) are required to describe subtle changes in the spectral absorption lines. With the detailed spectral features, a method was developed based on solar line fitting and the Beer-Lambertian law. This method is robust and accurate when the spectrum is out of the influence of telluric absorptions, even in the presence of aerosols (Frankenberg et al., 2011a; Joiner et al., 2011); in the current study, this method was applied to develop the IAPCAS/SIF algorithm. Another SIF retrieval method is the data-driven algorithm based on the singular value decomposition (SVD) technique (Joiner et al., 2011; Guanter et al., 2012), which has been broadly applied in GOSAT, OCO-2, TanSat and TROPOMI SIF retrieval (Joiner et al., 2011; Guanter et al., 2012, 2015; Frankenberg et al., 2014a; Du et al., 2018; Köhler et al., 2018b). In the data-driven method, the spectrum is represented as a linear combination of the SIF signal and several singular vectors that are trained from non-fluorescent scenes by SVD; thus, the SIF signal can be obtained with

111 linear least-squares fitting (Du et al., 2018; Guanter et al., 2012). The first TanSat SIF map was obtained by the SVD
112 method (Du et al., 2018). In a previous study, a new TanSat SIF product retrieved by IAPCAS/SIF algorithm was introduced
113 and the two kinds of TanSat SIF product by IAPCAS/SIF and SVD methods were compared. The preliminary comparison
114 between the two TanSat SIF products shows that the two SIF products share a similar global pattern and signal magnitude
115 for all seasons while different biases still exist in four seasons (Yao et al., 2021). The different biases in four seasons may be
116 caused by the different training samples of the SVD method, which indicates that the training samples have a significant
117 impact on the retrieval results. In order to obtain stable SIF data products from TanSat and other subsequent satellite
118 missions, it is particularly important to establish a stable and high-precision SIF inversion algorithm. To detailed validate the
119 IAPCAS/SIF algorithm and test the potential of comprehensive usage of multi-satellites SIF data in analysis, in this study,
120 we detailed the TanSat SIF retrieval using the IAPCAS/SIF algorithm and made a comparison of SIF products between
121 TanSat and OCO-2 in variety of temporal-spatial scales, although a preliminary test was shown in previous work.

2 Data and retrieval algorithm

2.1 Retrieval Principle and Method

124 We used TanSat version 2 Level 1B (L1B) nadir-mode earth observation data in the retrieval process. The measurements
125 covered the period from March 2017 to February 2018. Polarized radiance in the O_2-A band with a spectral resolution of
126 0.044 nm was provided in the L1B data, and two micro-windows near 757 nm (758.3-759.2 nm) and 771 nm (769.6-770.3
127 nm) were chosen to retrieve the top-of-atmosphere (TOA) SIF while avoiding the contamination from strong lines of
128 atmospheric gas absorption. The retrieval was independent for each micro-window as shown in Figure 1. To avoid
129 duplication of information, we use the SIF product at 757 nm as the example in the analysis.
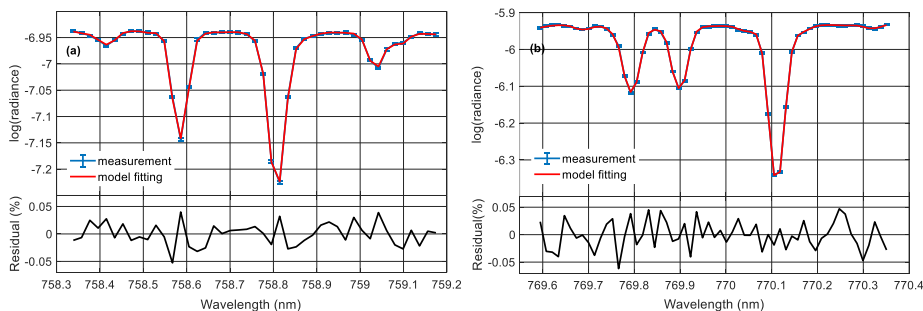
Figure 1: The fitted spectra and residuals for the (a) 757 nm and (b) 771 nm micro-windows of TanSat measurement. The error bar of the measured spectra depicts the estimated precision of each TanSat sounding.

删除的内容:),

删除的内容: in

删除的内容: a

删除的内容: retrieved by IAPCAS/SIF algorithm and the SVD data-driven method was performed, and the comparison

删除的内容: e

删除的内容: the

删除的内容: .

142 Filling-in on solar lines by chlorophyll fluorescence in the O_2-A band can be detected in the hyperspectral measurements
143 from TanSat. This effect on spectral radiance is different from the impact of atmospheric and surface processes, e.g.,
144 scattering and absorption. For example, scattering by aerosols and clouds does not change the relative depth of clear solar
145 lines, unlike the SIF emission signal. We applied the differential optical absorption spectroscopy (DOAS) technique to
146 IAPCAS/SIF algorithm for TanSat measurement (Frankenberg, 2014b; Sun et al., 2018).
147 The TOA spectral radiance (L_{TOA}^λ) at wavelength λ can be represented as follows:

148
$$L_{TOA}^\lambda = I_t^\lambda \cdot \mu_0 \cdot (\rho_0^\lambda + \frac{\rho_s^\lambda \cdot T_\downarrow^\lambda \cdot T_\uparrow^\lambda}{\pi}) + F_{TOA}^\lambda \tag{1}$$

149 where I_t^λ is the incident solar irradiance at the TOA, μ_0 is the cosine of the solar zenith angle (SZA), ρ_0^λ is atmospheric path
150 reflectance, ρ_s^λ is surface reflectance, and $T_\downarrow^\lambda$ and $T_\uparrow^\lambda$ are the total atmospheric transmittances along the light-path in the
151 downstream and upstream directions, respectively. F_{TOA}^λ is the SIF radiance at TOA.
152 The first term on the right of Eq. (1) represents the transmission process of solar radiance. In the micro-windows used in SIF
153 retrieval, gas absorption is very weak and smooth, and hence, the atmosphere term $\mu_0 \cdot (\rho_0^\lambda + \frac{\rho_s^\lambda \cdot T_\downarrow^\lambda \cdot T_\uparrow^\lambda}{\pi})$ can be simplified to a
154 low-order polynomial that varies with λ (Joiner et al., 2013; Sun et al., 2018); this is always valid as long as the spectrum
155 fitting range is out of sharp atmospheric absorptions. In the retrieval, the spectral radiance measurement was converted to
156 logarithmic space by the instrument and the radiative transfer process $f(F_s^{rel}, \boldsymbol{a})$ was represented as follows:

157
$$f(F_s^{rel}, \boldsymbol{a}) = log(< I_t + F_s^{rel} >) + \sum_{i=0}^{n} a_i \cdot \lambda^i \tag{2}$$

158 where $<>$ denote the convolution with the ISRF from line-by-line spectra. The polynomial coefficient $\boldsymbol{a}$ determines the
159 wavelength dependence polynomial for the atmosphere term; in the retrieval, we used a second-order polynomial ($n = 2$).
160 The radiance is normalized to the continuum level; hence, I_t is a normalized disk-integrated solar transmission model, and
161 F_s^{rel} is the normalized relative SIF. In the micro-window, SIF was regarded as a constant signal due to its small changes.
162 Although the atmospheric gas absorption was very weak in the micro-window, the weak absorption and the far-wing effects
163 (O_2 lines) can still change spectral features, which induces errors in spectrum fitting. In other physical-based retrievals, the
164 surface pressure data of the European Centre for Medium-Range Weather Forecasts (ECMWF) is usually used as the true
165 surface pressure to simulate the molecular absorption cross-section. However, there is still a difference between the true
166 surface pressure and the model surface pressure, so we introduced a factor here to reduce the influent of the inaccurate
167 surface pressure. In IAPCAS/SIF algorithm, we used the ECMWF interim surface pressure ($0.75° \times 0.75°$) to estimate O_2
168 absorption firstly and then modified the absorption feature by a scale factor. The scale factor is obtained simultaneously in
169 SIF retrieval to reduce the error induced by the uncertainty in surface pressure. As described by Yang (2020), there is also a
170 continuum feature in TanSat L1B data that needs to be considered for the high-quality fitting of the O_2-A band. However, in
171 this study, this continuum feature was not corrected, as the impact of such a smooth continuum variation in the micro-
172 window is weak and the polynomial continuum model is capable of compensating for most of this effect.

删除的内容: Therefore

删除的内容: European Centre for Medium-Range Weather Forecasts (

删除的内容:)

177   The state vector list in the retrieval includes the relative SIF signal F_s^{rel}, a wavenumber shift, the scale of O_2 column

178   absorption for surface pressure correction, and coefficients of the polynomial. The continuum level radiance I_{cont} within the

179   fitting window is calculated using the radiance outside the absorption features in the micro-window and is then used for the

180   actual SIF signal calculation thus: $F = F_s^{rel} \cdot I_{cont}$.

181   In the IAPCAS/SIF algorithm, we used an OEM for state vector optimization in the retrieval process. Unlike XCO_2 retrieval,

182   SIF retrieval employs a state vector with fewer elements and a much simpler forward model, so there is no need to perform

183   complex radiation transmission calculations. Considering the low complexity of SIF retrieval, the Gauss-Newton method

184   was applied in inversion iteratively to find the optimal solution.

185   **2.2 Bias Corrections**

186   A systematic error remains in the raw SIF retrieval output if no bias correction is performed; similar results have been

187   reported in GOSAT and OCO-2 SIF retrieval studies (Frankenberg et al., 2011a, 2011b; Sun et al., 2018). This is because the

188   SIF signal is weak (e.g., typically ~1-2% of the continuum level radiance), which means that even a small issue in the

189   measurement, such as a zero-offset caused by radiometric calibration error, could induce significant bias. Unfortunately, the

190   lack of knowledge on in-flight instrument performance makes it difficult to perform a direct systematic bias correction in the

191   measured spectrum. In the retrieval, a continuum level radiance bin fit was used to estimate the bias. The bins have a

192   continuum level radiance interval of 5 W $m^{-2}\,\mu m^{-1}$ sr^{-1}. In each bin, the mean bias was estimated using all non-fluorescence

193   measurements, and a piecewise linear function was built from the mean bias of each continuum level radiance interval.

194   The non-fluorescence soundings that were used in the bias estimation were based on the dataset "sounding_landCover" in

195   TanSat L1B data. This dataset depends on the MODIS land cover product and provides a scheme consisting of 17 land cover

196   classifications defined by the International Geosphere-Biosphere Programme. These retrieved measurements marked as

197   "snow and ice," "barren," and "sparsely vegetated" were chosen to estimate the bias. Calibrations compensated for most of

198   the instrument degradations, but this alone was not perfect. To reduce the impact from the remaining minor discrepancies,

199   we built the bias correction function daily to obtain bias for each sounding via interpolation of the continuum level radiance

200   (Sun et al., 2017b, 2018).

201   The bias curves shown in Figure 2 differ significantly between TanSat and OCO-2. This is mostly due to the differences in

202   instrument performance and radiometric calibration. In general, the TanSat bias curves exhibited two peaks at radiance levels

203   of approximately 40 and 125 W $m^{-2}\,\mu m^{-1}$ sr^{-1}, separately, and most biases were larger than 0.015. For OCO-2, the curves

204   dropped sharply at low radiance levels, reaching the valley at a radiance level of approximately 40 W $m^{-2}\,\mu m^{-1}$ sr^{-1}, and then

205   increased slowly with the radiance level.
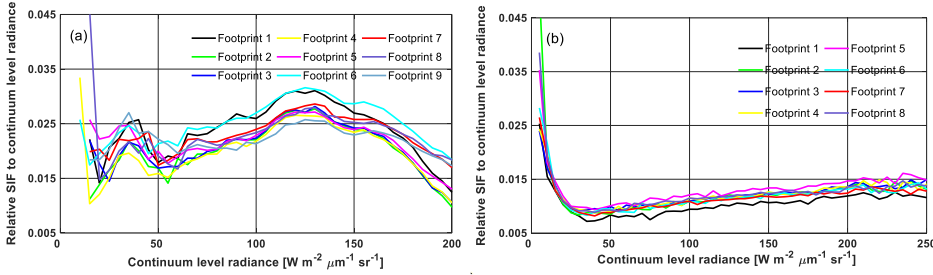
Figure 2: Variations in the bias correction curves of continuum level radiance from (a) TanSat on July 7, 2017, and (b) Orbiting Carbon Observatory-2 (OCO-2) on June 16, 2017. The different colors in the legend present different footprints of the satellite frame.

2.3 Data Quality Controls

Only data that passed quality control were used in further applications. There were two data quality control processes for the SIF products: pre-screening and post-screening. Pre-screening focused mainly on cloud screening; only cloud-free measurements were used in SIF retrieval. A surface pressure difference (SPD), defined as:

$$\Delta P_0 = |P_{retrieval} - P_{ECMWF}| \tag{3}$$

was used to evaluate cloud contamination along with a chi-square test

$$\chi^2 = \sum \frac{(y_{sim} - y_{obs})^2}{y_{noise}^2} \tag{4}$$

where y_{sim}, y_{obs}, and y_{noise} represent the model fitting spectrum, observation spectrum, and spectrum noise, respectively. $P_{retrieval}$ is the apparent surface pressure obtained from O_2-A band surface pressure retrieval, assuming a single scattering atmosphere. P_{ECMWF} is the ECMWF interim ($0.75° \times 0.75°$) surface pressure. A "cloud-free" measurement was required to simultaneously satisfy an SPD of less than 20 hPa and a χ^2 value of less than 80. Here, post-screening was applied to filter out "bad" retrievals; this screening process involved the following steps: (1) SIF retrievals with reduced χ^2 (χ_{red}^2) values ranging from 0.7 to 1.3 were considered "good" fitting, (2) continuum level radiance outside the range of 15 ~ 200 W m^{-2} μm^{-1} sr^{-1} was screened out to avoid scenes too bright or too dark, and (3) soundings with the SZA higher than 60° were also filtered out.

2.4 IAPCAS versus IMAP-DOAS OCO-2 SIF Retrieval

Before applied to TanSat retrievals, we tested the IAPCAS/SIF algorithm on the OCO-2 L1B data first (OCO2_L1B_Science.8r) and then compared the retrieval results with the OCO-2 L2 Lite SIF product (OCO2_Level 2_Lite_SIF.8r) retrieved by the Iterative Maximum A Posteriori-Differential Optical Absorption Spectroscopy (IMAP-DOAS) algorithm (Frankenberg, 2014b). The Lite product provides the SIF value for each sounding on a daily basis and hence the SIF comparison could be performed on the sounding scale for each month.

Table 1 displays the relationship of OCO-2 SIF values between the IAPCAS/SIF and IMAP-DOAS at 757 nm micro-window for each month. Overall, the two SIF products were in good agreement. The linear fitting of the two SIF products suggests that they are highly correlated, as indicated by the strong linear relationship with R^2 mostly larger than 0.85 and the root mean square error (RMSE) of about 0.2 W m^{-2} μm^{-1} sr^{-1}. Good consistency between the two SIF products implies the reliability of the IAPCAS/SIF algorithm; thus, it was further applied to TanSat SIF retrieval. However, there was still a small bias in the comparisons, which was due, most likely, to the impact of differences in the bias correction method, retrieval algorithm, and fitting window.

Table 1: Summary of the relationship between the Institute of Atmospheric Physics Carbon Dioxide Retrieval Algorithm for Satellite Remote Sensing (IAPCAS) OCO-2 and Iterative Maximum A Posteriori-Differential Optical Absorption Spectroscopy (IMAP-DOAS) OCO-2 solar-induced chlorophyll fluorescence (SIF) products at 757nm micro-window.

month	Number of soundings	Slope	Intercept	R^2	RMSE/ W m^{-2} μm^{-1} sr^{-1}
2017/03	1097277	0.85	0.034	0.86	0.18
2017/04	1119464	0.86	0.045	0.87	0.19
2017/05	1054235	0.88	0.041	0.88	0.19
2017/06	1014848	0.91	0.032	0.90	0.19
2017/07	965309	0.92	0.011	0.91	0.19
2017/09	211219	0.88	0.005	0.81	0.23
2017/10	473359	0.88	0.031	0.88	0.17
2017/11	579009	0.87	0.022	0.85	0.19
2017/12	645134	0.87	0.020	0.88	0.16
2018/01	788655	0.87	0.019	0.88	0.17
2018/02*	629995	0.86	0.024	0.87	0.18

* Due to the lack of OCO-2 measurements in August 2017, the comparison is only performed for 11 months.

3 Results and Discussion

3.1 Comparison between TanSat and OCO-2 SIF Measurements

The comparison between TanSat and OCO-2 SIF Measurements is a useful and powerful method for further verification of the IAPCAS/SIF algorithm. The reason for adopting OCO-2 data is that OCO-2 and TanSat have similar observation modes, including scanning method, transit time, spatial resolution, spectral resolution, and spectral range. The similarities mean that the SIF product from the two satellite missions can be directly compared. Directly comparing OCO-2 and TanSat SIF measurements could provide information on joint data application at the sounding scale for further studies. However, an identical sounding overlap barely exists because the two satellites often have different nadir tracks on the ground, which is induced by the different temporal and spatial intervals of the two satellite missions. Fortunately, the ground tracks of the two satellites were relatively close from April 17 to April 23, 2017. A couple of overlapping orbits were found in the measurements obtained from Africa with the orbit number of 1733 from TanSat and 14890a from OCO-2 (Figure 3). In the

253 comparison, the OCO2_Level 2_Lite_SIF.8r product was used to present the SIF emission over the study area. These
254 overlapping measurements encompassed multiple land cover types, in which the SIF varied within an acceptable time
255 difference (<5 min).
256 Overall, measurements from the two satellites indicated SIF variation with land cover type. The SIF emission over evergreen
257 broadleaf forests was larger than that over savannas, and grasslands exhibited the lowest SIF emission in April (Figure 3a,b).
258 The mean SIF emission over evergreen broadleaf forests was approximately 0.9-1.1 W m^{-2} μm^{-1} sr^{-1}, whereas those over
259 savannas and grasslands were 0.5-0.7 W m^{-2} μm^{-1} sr^{-1} and less than 0.1 W m^{-2} μm^{-1} sr^{-1}, respectively (Figure 3c,d).
260 Furthermore, we also found a significant difference in the SIF emission intensity over tropical savannas, which was observed
261 by both satellites (Figure 3c,d).
262
263

264
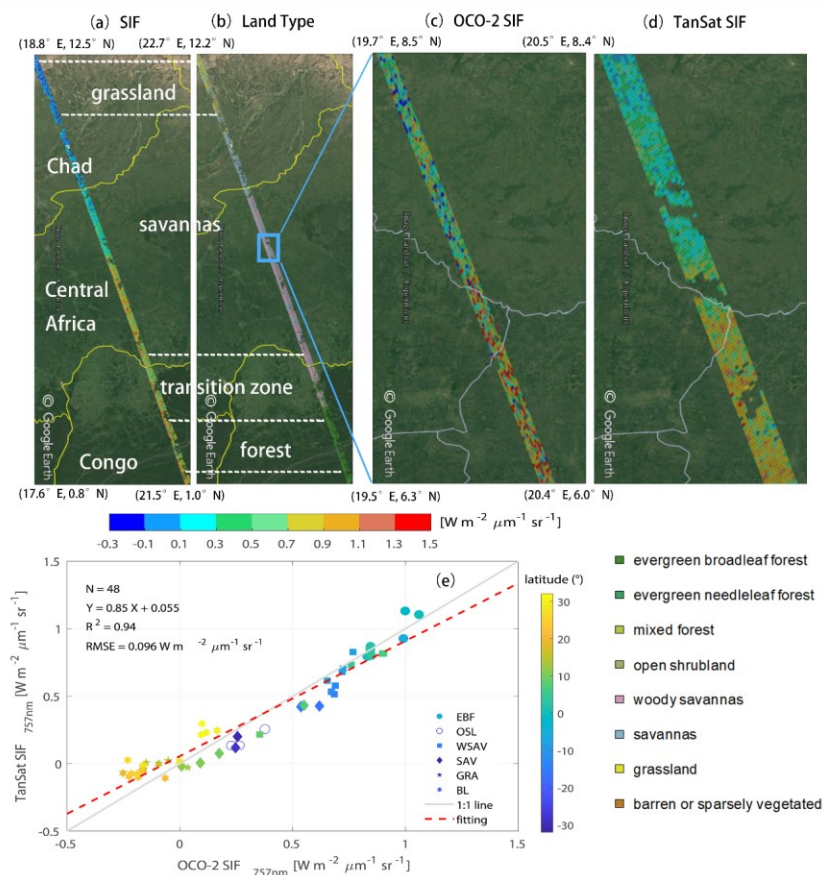
Figure 3: Overlapping orbits of TanSat and OCO-2 on April 19, 2017 over Africa displayed in Google Earth, (a) the SIF measurements from both the two satellites and (b) the footprint land cover type were compared. Compared to OCO-2, TanSat has a wider swath width. A zoom-in view over savannas shows variations in the SIF signal measured by (c) OCO-2 and (d) TanSat. The land surface image shown in Google earth is provided by Landsat/Copernicus team. Following the International Geosphere-Biosphere Programme classification scheme, the vertical legend on the bottom right corner depicts the land cover type that occurs in the study area. The middle horizontal color bar represents the intensity of the SIF radiance. (e) Small-area SIF comparison between OCO-2 and TanSat; each data point represents the mean SIF of a degree in latitude (colors) along the track. The marker legend that is shown on the bottom right of the plot indicates the dominant land cover (defined as the majority land cover type of each sounding) in each small area. There are six land cover types including evergreen broadleaf forest (EBF), open shrubland (OSL), woody savanna (WSAV), savanna (SAV), grassland (GRA), and barren land (BL). The red dashed line represents the linear fit between the two SIF products with statistics shown in the upper left of the plot. The gray line indicates a 1:1 relationship for reference.

277

278 Because the footprint sizes of the two satellites are different, it is difficult to make a direct footprint-to-footprint comparison.

279 Therefore, we made the comparison between the two satellite measurements based on a small area average. Each small area

280 spans a degree in latitude and continues along the track. The small area-averaged SIF comparison is shown in Figure 3e. The

281 results indicate good agreement, with an R^2 of 0.94 and an RMSE of 0.096 W m^{-2} μm^{-1} sr^{-1}. Additional ground-based SIF

282 measurement setups (Guanter et al., 2007; Liu et al., 2019; van der Tol et al., 2016; Yang et al., 2015a; Yu et al., 2019)

283 should allow for direct evaluation of satellite retrieval accuracy in the future.

284
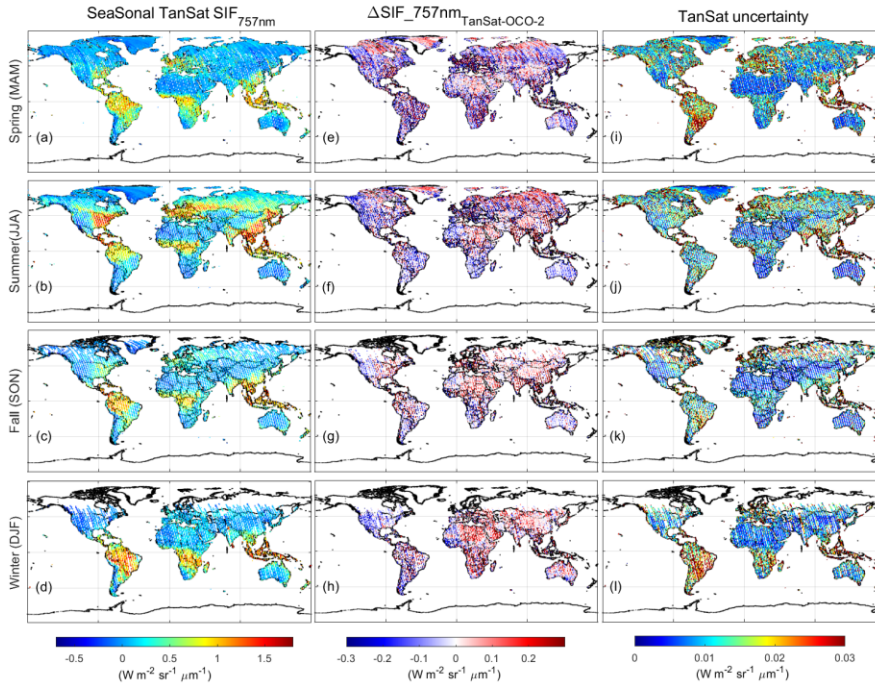
285

286 **Figure 4: Global TanSat SIF (left, a-d), differences between TanSat and IAPCAS OCO-2 SIF values (middle, e-h), and the grid-**
287 **cell retrieval uncertainty estimated from TanSat (right, i-l) at 1° × 1° spatial resolution. The maps in each row represent a**
288 **Northern Hemisphere season, i.e., spring (MAM), summer (JJA), fall (SON), and winter (DJF).**

289

290   Figure 4 shows the global SIF comparison between IAPCAS/SIF retrieved OCO-2 and TanSat; this comparison is only
291   performed at 1° × 1° spatial resolution. In general, the difference in SIF globally is mostly less than 0.3 W m^{-2} μm^{-1} sr^{-1} for
292   all seasons, and on average, the smallest difference appears in fall. There are regional biases observed in North Africa, South
293   Africa, South America, and Europe in all seasons except fall. This is mainly caused by the differences in instrument
294   performance between TanSat and OCO-2, such as the Instrument Respond Function and the Signal-to-Noise. The instrument
295   performance difference is represented by the different structural characteristics of the bias curves. The bias correction
296   compensates for most of the bias caused by instrument performance; however, small biases could remain. Furthermore, the
297   hundreds of kilometers of distance between the OCO-2 and TanSat footprints, for example, over different vegetation regions,
298   will also cause some measurement discrepancies. The global distribution of the two satellites was also compared with the
299   official OCO-2 SIF data on the global scale, the results show that the difference between the retrieved SIF maps and the
300   official map is less than 0.2 W m^{-2} μm^{-1} sr^{-1}, indicating that the retrieved SIF data from OCO-2 and TanSat both have good
301   SIF characterization capabilities on a global scale. The uncertainty σ of each sounding was estimated to validate SIF
302   reliability and is provided in the product. σ is derived from the retrieval error covariance matrix, $S_e = (K^T S_0^{-1} K)^{-1}$, where K
303   is the Jacobian matrix from the forward model fitting and S_0 is the measurement error covariance matrix that is calculated
304   from the instrument spectrum noise. In general, σ ranges from 0.1 to 0.6 W m^{-2} μm^{-1} sr^{-1} for both TanSat and OCO-2
305   measurements in the 757 nm fitting window, which is of a similar magnitude and data range as those of previous studies (Du
306   et al., 2018; Frankenberg et al., 2014a). Meanwhile, the standard error of the mean SIF in each grid σ_{meas} was estimated to
307   represent the gridded retrieval error and natural variability, which is calculated from TanSat SIF values with $\sigma_{meas} = \frac{\sigma_{std}}{\sqrt{n}}$

308   and $\sigma_{std} = \sqrt{\frac{\sum_{i=1}^{n}(SIF_i - \overline{SIF})^2}{n}}$, where σ_{std} represents the standard deviation of the grid cell with n soundings, SIF_i is the
309   retrieved SIF values of each sounding, and $\overline{SIF}$ is the mean SIF value for all measurements in the grid. As depicted in the
310   right column of Figure 4, the σ_{meas} of each grid cell is much lower than the precision of a single sounding. The σ_{meas} for
311   South America is larger than that for any other region on the globe (Figure 4i-l). This is similar to that of OCO-2 SIF
312   retrieval and caused by fewer effective measurements due to the South Atlantic Anomaly (Sun et al., 2018). The difference
313   in SIF emission values between the two satellites indicates that the collaborative usage of two satellite SIF products still
314   requires analysis of the impact of instrument differences, although the two satellite SIF products share the same
315   spatiotemporal pattern on a global scale.

316   **3.2 SIF Global Distribution and Temporal Variation**

317   The SIF emission intensity reflects the growth status of vegetation due to its correlation with photosynthetic efficiency;
318   hence, the overall global vegetation status can be represented by global SIF maps for each season. TanSat SIF over a whole
319   year's cycle, from March 2017 to February 2018, is represented seasonally as a 1° × 1° grid spatially. The seasonal variation

320 in SIF emission is clear in the Northern Hemisphere, i.e., it is enhanced from spring to summer and then decreases (Sun et al.,
321 2018).

322 In general, the SIF emission varied with latitude and the vegetation-covered areas near the equator maintained a continuous
323 SIF emission throughout the year. Large SIF emissions in the Northern Hemisphere, above 1.5 W m^{-2} μm^{-1} sr^{-1}, mostly from
324 the eastern U.S., southeast of China, and southern Asia in summer, were due to the large areas of cropland. There was also
325 an obvious SIF emission of 1-1.2 W m^{-2} μm^{-1} sr^{-1} observed over Central Europe and northeastern China during the summer.
326 In these regions, croplands and deciduous forests contribute to SIF emissions. In the Southern Hemisphere, the strongest SIF
327 emission occurred in the Amazon, with a level of approximately 1-2 W m^{-2} μm^{-1} sr^{-1} in DJF (Northern Hemisphere winter),
328 where there is an evergreen broadleaf rainforest. Africa, which is covered by evergreen broadleaf rainforests and woody
329 savannas, had an average SIF value of 0.7-1.5 W m^{-2} μm^{-1} sr^{-1} during the year.

330 The SIF-GPP relationship over different vegetation types was also investigated by comparing the annual mean satellite SIF
331 measurements with the FLUXCOM GPP (Jung et al., 2020; Tramontana et al., 2016) dataset in a 1° × 1° grid over the globe.
332 The FLUXCOM GPP dataset used in the study comprises monthly global gridded flux products with remote sensing and
333 meteorological/climate forcing (RS+METEO) setups, which are derived from mean seasonal cycles according to MODIS
334 data and daily meteorological information (Jung et al., 2020; Tramontana et al., 2016). In the correlation analysis, the high
335 spatial resolution (0.5°× 0.5°) of the FLUXCOM GPP was first resampled to 1°× 1° to keep the same temporal-spatial scale
336 of SIF and GPP data. The satellite-measured SIF is an instantaneous emission signal that varies with incident solar radiance
337 within the day. To reduce the differences caused by the observation time and SZA at different latitudes, we applied a daily
338 adjustment factor to convert the instantaneous SIF emission into a daily mean SIF (Du et al., 2018; Frankenberg et al., 2011b;
339 Sun et al., 2018). The daily adjustment factor d is calculated as follows:

340
$$d = \frac{\int_{t=t_0-12h}^{t=t_0+12h} cos\,(SZA(t)) \cdot dt}{cos(SZA(t_0))} \tag{5}$$

341 where t_0 is the observation time in fractional days and $SZA(t)$ is a function of latitude, longitude, and time for calculating
342 the SZA of the measurements. The annual averaged SIF is calculated from the daily mean SIF. To evaluate the relationship
343 between SIF and GPP on the periodic scale of vegetation growth status, annually-averaged data were used in the regression
344 fitting analysis.

345
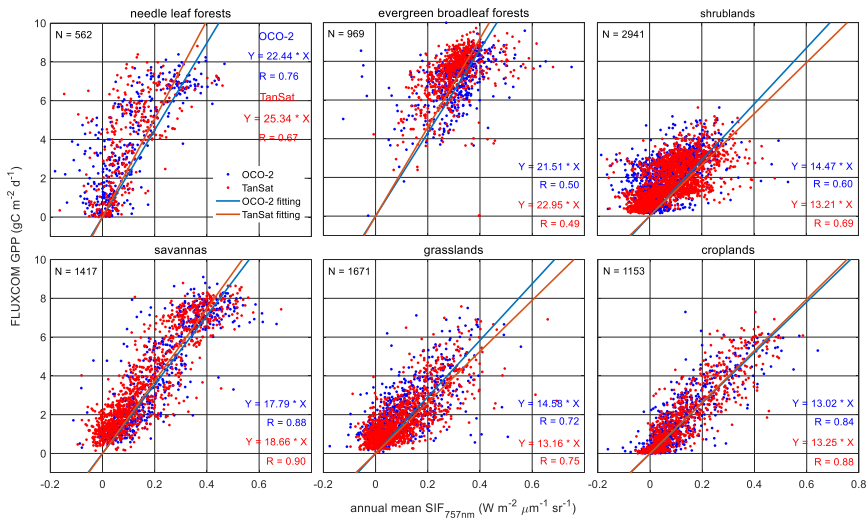
Figure 5: Relationship between annual mean SIF and FLUXCOM gross primary production (GPP) from March 2017 to February 2018. Blue and red dots represent OCO-2 and TanSat SIF grids, respectively. Fitted lines and statistics for OCO-2 and TanSat are shown in each plot.

Figure 5 shows the linear fits for six vegetation types, including needle leaf forest, evergreen broadleaf forest, shrubland, savanna, grassland, and cropland. Recent studies have shown a strong linear correlation between SIF and GPP. The TanSat SIF and the OCO-2 official SIF data were used to estimate the SIF-GPP correlation. To make a direct comparison of the relationship between SIF and GPP among various vegetation types, we used non-offset linear fitting to indicate the correlation between satellite SIF and FLUXCOM GPP. For savanna and cropland, there were strong relationships between the mean SIF and GPP with an R-value above 0.84. The fitting results show that the SIF products of the two satellites have similar capabilities in characterizing GPP, especially for the evergreen broadleaf forest, savanna, and cropland, with slopes of approximately 21, 18, and 13, respectively. For shrubland and grassland, the slope of OCO-2 SIF with GPP is higher than that of TanSat and has a worse correlation. For forests, OCO-2 SIF presents a better correlation with GPP, especially in the needle leaf forest. As a whole, for the same vegetation type, the SIF-GPP correlations for the two satellites are rather similar, indicating that the two satellite SIF products have similar capabilities in characterizing GPP. It shows the strong feasibility of the comprehensive application of different satellite SIF products. For different vegetation types, the SIF-GPP correlations were significantly different, indicating the different ability of SIF to characterize GPP of different vegetation. It represents that vegetation type is a key factor in determining the SIF-GPP relationship. The markedly different fitting slopes across various biomes suggest that the application of SIF in GPP estimation needs more detailed analysis although the evidence of the strong linear relationship between them.

删除的内容: estimation

366 **4 Conclusions**

367 In this paper, we introduced the retrieval algorithm IAPCAS/SIF and its application in TanSat and OCO-2 measurements.
368 One-year (March 2017-February 2018) TanSat SIF data was introduced and compared with OCO-2 measurements in this
369 study. The TanSat and OCO-2 SIF products based on the IAPCAS/SIF algorithm are available on the Cooperation on the
370 Analysis of carbon SAtellites data (CASA) website, www.chinageoss.org/tansat. Comparisons between TanSat and OCO-2
371 measurements directly, using a case study, and indirectly, with global $1° \times 1°$ grid data, showed consistency between the two
372 satellite missions, indicating that the coordinated usage of the two data products is possible in future studies. The correlation
373 analysis between SIF and GPP further verified the feasibility of the comprehensive application of SIF products from
374 different satellite missions. Meanwhile, it should be noticed that the difference in the ability of satellite SIF products to
375 characterize different vegetation types in data applications. With increasing satellites becoming available for SIF
376 observations, space-based SIF observations have recently expanded in range to provide broad spatiotemporal coverage. The
377 next-generation Chinese carbon monitoring satellite (TanSat-2) is now in the preliminary design phase, which is designed to
378 be a constellation of six satellites to measure different kinds of greenhouse gases and trace gases in a more efficient way,
379 including CO_2, CH_4, CO, NOx, as well as SIF. SIF measurements from TanSat-2 will provide global data products over
380 broader coverage areas with less noise. The improvement in the spatiotemporal resolution of SIF data will benefit GPP
381 predictions based on the numerous studies of the linear relationship between SIF and GPP. In future work, the measurement
382 accuracy should be validated directly using ground-based measurements to ensure data quality.

383 **Data availability**

384 The SIF products of TanSat and OCO-2 by IAPCAS/SIF algorithm are available on the Cooperation on the Analysis of
385 carbon SAtellites data (CASA) website (www.chinageoss.org/tansat).
386

387 **Author contributions**

388 L.Y. and D.Y. developed the retrieval algorithm, designed the study, and wrote the paper. Y.L. led the SIF data process and
389 analysis. Y.L., D.Y., Z.C., and J.W. contributed to manuscript organization and revision. C.L. and Y.Z. provided information
390 on the TanSat instrument performance. L.T. provided TanSat in-flight information. M.W. and S.W. provided information on
391 the scientific requirement for data further application. N.L. and D.L. led the TanSat data application. Z.Y. led the TanSat in-
392 flight operation.

393 **Competing interests**

394 The authors declare that they have no conflict of interest.

395 **Acknowledgments**

396 The TanSat L1B data service was provided by the International Reanalysis Cooperation on Carbon Satellites Data (IRCSD)
397 and the Cooperation on the Analysis of carbon SAtellites data (CASA). The authors thank OCO-2 Team for providing
398 Level-1B data and Level-2 SIF data products. The authors thank the FLUXCOM team for providing global GPP data. The
399 authors thank Google for allowing free use of Google Earth and reproduction of maps for publication. The authors also thank
400 the Landsat/Copernicus team for providing land surface images for Google Earth.

401 **Financial support**

402 This work has been supported by the Key Research Program of the Chinese Academy of Sciences (ZDRW-ZS-2019-1), and
403 the Youth Program of the National Natural Science Foundation of China (41905029).

404 **References**

405 Boesche, E., Stammes, P., and Bennartz, R.: Aerosol influence on polarization and intensity in near-infrared O_2 and CO_2
406 absorption bands observed from space, J. Quant. Spectrosc. Radiat. Transf., 110, 223–239,
407 https://doi.org/10.1016/j.jqsrt.2008.09.019, 2009.

408 Butz, A., Guerlet, S., Hasekamp, O., Schepers, D., Galli, A., Aben, I., Frankenberg, C., Hartmann, J. M., Tran, H., Kuze, A.,
409 Keppel-Aleks, G., Toon, G., Wunch, D., Wennberg, P., Deutscher, N., Griffith, D., MacAtangay, R., Messerschmidt, J.,
410 Notholt, J., and Warneke, T.: Toward accurate CO_2 and CH_4 observations from GOSAT, Geophys. Res. Lett., 38, 2–7,
411 https://doi.org/10.1029/2011GL047888, 2011.

412 Butz, A., Hasekamp, O. P., Frankenberg, C., and Aben, U.: Retrievals of atmospheric CO_2 from simulated space-borne
413 measurements of backscattered near-infrared sunlight: Accounting for aerosol effects, Appl. Opt., 48, 3322–3336,
414 https://doi.org/10.1364/AO.48.003322, 2009.

415 Butz, A., Hasekamp, O. P., Frankenberg, C., Vidot, J., and Aben, I.: CH_4 retrievals from space-based solar backscatter
416 measurements: Performance evaluation against simulated aerosol and cirrus loaded scenes, J. Geophys. Res. Atmos., 115, 1–
417 15, https://doi.org/10.1029/2010JD014514, 2010.

418 Cai, Z. N., Liu, Y., and Yang, D. X.: Analysis of XCO_2 retrieval sensitivity using simulated Chinese Carbon Satellite
419 (TanSat) measurements, Sci. China Earth Sci., 57, 1919–1928, https://doi.org/10.1007/s11430-013-4707-1, 2014.

Chen, A., Mao, J., Ricciuto, D., Xiao, J., Frankenberg, C., Li, X., Thornton, P. E., Gu, L., and Knapp, A. K.: Moisture availability mediates the relationship between terrestrial gross primary production and solar-induced chlorophyll fluorescence: Insights from global-scale variations, Glob. Chang. Biol., 1–13, https://doi.org/10.1111/gcb.15373, 2020.

Doughty, R., Köhler, P., Frankenberg, C., Magney, T. S., Xiao, X., Qin, Y., Wu, X., and Moore, B.: TROPOMI reveals dry-season increase of solar-induced chlorophyll fluorescence in the Amazon forest, Proc. Natl. Acad. Sci. U. S. A., 116, 22393–22398, https://doi.org/10.1073/pnas.1908157116, 2019.

Drusch, M., Moreno, J., del Bello, U., Franco, R., Goulas, Y., Huth, A., Kraft, S., Middleton, E. M., Miglietta, F., Mohammed, G.: The FLuorescence EXplorer Mission Concept—ESA's Earth Explorer 8, ITGRS, 55, 1273–1284, http://doi.org./10.1109/TGRS.2016.2621820, 2017.

Du, S., Liu, L., Liu, X., Zhang, X., Zhang, X., Bi, Y., and Zhang, L.: Retrieval of global terrestrial solar-induced chlorophyll fluorescence from TanSat satellite, Sci. Bull., 63, 1502–1512, https://doi.org/10.1016/j.scib.2018.10.003, 2018.

Frankenberg, C., Butz, A., and Toon, G. C.: Disentangling chlorophyll fluorescence from atmospheric scattering effects in O2 A-band spectra of reflected sunlight, Geophys. Res. Lett., 38, 1–5, https://doi.org/10.1029/2010GL045896, 2011a.

Frankenberg, C., Fisher, J. B., Worden, J., Badgley, G., Saatchi, S. S., Lee, J. E., Toon, G. C., Butz, A., Jung, M., Kuze, A., and Yokota, T.: New global observations of the terrestrial carbon cycle from GOSAT: Patterns of plant fluorescence with gross primary productivity, Geophys. Res. Lett., 38, 1–6, https://doi.org/10.1029/2011GL048738, 2011b.

Frankenberg, C., O'Dell, C., Berry, J., Guanter, L., Joiner, J., Köhler, P., Pollock, R., and Taylor, T. E.: Prospects for chlorophyll fluorescence remote sensing from the Orbiting Carbon Observatory-2, Remote Sens. Environ., 147, 1–12, https://doi.org/10.1016/j.rse.2014.02.007, 2014a.

Frankenberg, C., O'Dell, C., Guanter, L., and McDuffie, J.: Remote sensing of near-infrared chlorophyll fluorescence from space in scattering atmospheres: Implications for its retrieval and interferences with atmospheric CO 2 retrievals, Atmos. Meas. Tech., 5, 2081–2094, https://doi.org/10.5194/amt-5-2081-2012, 2012.

Frankenberg, C.: OCO-2 Algorithm Theoretical Basis Document: IMAP-DOAS pre-processor, 2014b.

Guanter, L., Aben, I., Tol, P., Krijger, J. M., Hollstein, A., Köhler, P., Damm, A., Joiner, J., Frankenberg, C., and Landgraf, J.: Potential of the TROPOspheric Monitoring Instrument (TROPOMI) onboard the Sentinel-5 Precursor for the monitoring of terrestrial chlorophyll fluorescence, https://doi.org/10.5194/amt-8-1337-2015, 2015.

Guanter, L., Alonso, L., Gómez-Chova, L., Amorós-López, J., Vila, J., and Moreno, J.: Estimation of solar-induced vegetation fluorescence from space measurements, Geophys. Res. Lett., 34, 1–5, https://doi.org/10.1029/2007GL029289, 2007.

Guanter, L., Frankenberg, C., Dudhia, A., Lewis, P. E., Gómez-Dans, J., Kuze, A., Suto, H., and Grainger, R. G.: Retrieval and global assessment of terrestrial chlorophyll fluorescence from GOSAT space measurements, Remote Sens. Environ., 121, 236–251, https://doi.org/10.1016/j.rse.2012.02.006, 2012.

Guanter, L., Zhang, Y., Jung, M., Joiner, J., Voigt, M., Berry, J. A., Frankenberg, C., Huete, A. R., Zarco-Tejada, P., Lee, J. E., Moran, M. S., Ponce-Campos, G., Beer, C., Camps-Valls, G., Buchmann, N., Gianelle, D., Klumpp, K., Cescatti, A.,

454 Baker, J. M., and Griffis, T. J.: Global and time-resolved monitoring of crop photosynthesis with chlorophyll fluorescence,
455 Proc. Natl. Acad. Sci. U. S. A., 111, https://doi.org/10.1073/pnas.1320008111, 2014.

456 Joiner, J., Guanter, L., Lindstrot, R., Voigt, M., Vasilkov, A. P., Middleton, E. M., Huemmrich, K. F., Yoshida, Y., and
457 Frankenberg, C.: Global monitoring of terrestrial chlorophyll fluorescence from moderate-spectral-resolution near-infrared
458 satellite measurements: methodology, simulations, and application to GOME-2, Atmos. Meas. Tech., 6, 2803–2823,
459 https://doi.org/10.5194/amt-6-2803-2013, 2013.

460 Joiner, J., Yoshida, Y., Guanter, L., and Middleton, E. M.: New methods for the retrieval of chlorophyll red fluorescence
461 from hyperspectral satellite instruments: simulations and application to GOME-2 and SCIAMACHY, Atmos. Meas. Tech., 9,
462 3939–3967, https://doi.org/10.5194/amt-9-3939-2016, 2016.

463 Joiner, J., Yoshida, Y., Vasilkov, A. P., Middleton, E. M., Campbell, P. K. E., Yoshida, Y., Kuze, A., and Corp, L. A.:
464 Filling-in of near-infrared solar lines by terrestrial fluorescence and other geophysical effects: simulations and space-based
465 observations from SCIAMACHY and GOSAT, Atmos. Meas. Tech., 5, 809–829, https://doi.org/10.5194/amt-5-809-2012,
466 2012.

467 Joiner, J., Yoshida, Y., Vasilkov, A. P., Yoshida, Y., Corp, L. A., and Middleton, E. M.: First observations of global and
468 seasonal terrestrial chlorophyll fluorescence from space, 8, 637–651, https://doi.org/10.5194/bg-8-637-2011, 2011.

469 Joiner, J., Yoshida, Y., Zhang, Y., Duveiller, G., Jung, M., Lyapustin, A., Wang, Y., and Tucker, C. J.: Estimation of
470 terrestrial global gross primary production (GPP) with satellite data-driven models and eddy covariance flux data, Remote
471 Sens., 10, 1–38, https://doi.org/10.3390/rs10091346, 2018.

472 Jung, M., Schwalm, C., Migliavacca, M., Walther, S., Camps-Valls, G., Koirala, S., Anthoni, P., Besnard, S., Bodesheim, P.,
473 Carvalhais, N., Chevallier, F., Gans, F., S Goll, D., Haverd, V., Köhler, P., Ichii, K., K Jain, A., Liu, J., Lombardozzi, D., E
474 M S Nabel, J., A Nelson, J., O'Sullivan, M., Pallandt, M., Papale, D., Peters, W., Pongratz, J., Rödenbeck, C., Sitch, S.,
475 Tramontana, G., Walker, A., Weber, U., and Reichstein, M.: Scaling carbon fluxes from eddy covariance sites to globe:
476 Synthesis and evaluation of the FLUXCOM approach, 17, 1343–1365, https://doi.org/10.5194/bg-17-1343-2020, 2020.

477 Köhler, P., Frankenberg, C., Magney, T. S., Guanter, L., Joiner, J., and Landgraf, J.: Global Retrievals of Solar-Induced
478 Chlorophyll Fluorescence With TROPOMI: First Results and Intersensor Comparison to OCO-2, Geophys. Res. Lett., 45,
479 10,456-10,463, https://doi.org/10.1029/2018GL079031, 2018b.

480 Köhler, P., Guanter, L., and Joiner, J.: A linear method for the retrieval of sun-induced chlorophyll fluorescence from
481 GOME-2 and SCIAMACHY data, Atmos. Meas. Tech., 8, 2589–2608, https://doi.org/10.5194/amt-8-2589-2015, 2015.

482 Köhler, P., Guanter, L., Kobayashi, H., Walther, S., and Yang, W.: Assessing the potential of sun-induced fluorescence and
483 the canopy scattering coefficient to track large-scale vegetation dynamics in Amazon forests, Remote Sens. Environ., 204,
484 769–785, https://doi.org/10.1016/j.rse.2017.09.025, 2018a.

485 Lee, J. E., Frankenberg, C., Van Der Tol, C., Berry, J. A., Guanter, L., Boyce, C. K., Fisher, J. B., Morrow, E., Worden, J. R.,
486 Asefi, S., Badgley, G., and Saatchi, S.: Forest productivity and water stress in Amazonia: Observations from GOSAT
487 chlorophyll fluorescence, Tohoku J. Exp. Med., 230, https://doi.org/10.1098/rspb.2013.0171, 2013.

488 Li, X., Xiao, J., and He, B.: Chlorophyll fluorescence observed by OCO-2 is strongly related to gross primary productivity
489 estimated from flux towers in temperate forests, Remote Sens. Environ., 204, 659–671,
490 https://doi.org/10.1016/j.rse.2017.09.034, 2018.

491 Li, X., Xiao, J., Kimball, J. S., Reichle, R. H., Scott, R. L., Litvak, M. E., Bohrer, G., and Frankenberg, C.: Synergistic use of
492 SMAP and OCO-2 data in assessing the responses of ecosystem productivity to the 2018 U.S. drought, Remote Sens.
493 Environ., 251, 112062, https://doi.org/10.1016/j.rse.2020.112062, 2020.

494 Liu, X., Guanter, L., Liu, L., Damm, A., Malenovský, Z., Rascher, U., Peng, D., Du, S., and Gastellu-Etchegorry, J. P.:
495 Downscaling of solar-induced chlorophyll fluorescence from canopy level to photosystem level using a random forest model,
496 Remote Sens. Environ., 231, 110772, https://doi.org/10.1016/j.rse.2018.05.035, 2019.

497 Liu, Y., Wang, J., Yao, L., Chen, X., Cai, Z., Yang, D., Yin, Z., Gu, S., Tian, L., Lu, N., and Lyu, D.: The TanSat mission:
498 preliminary global observations, Sci. Bull., 63, 1200–1207, https://doi.org/10.1016/j.scib.2018.08.004, 2018.

499 MacBean, N., Maignan, F., Bacour, C., Lewis, P., Peylin, P., Guanter, L., Köhler, P., Gómez-Dans, J., and Disney, M.:
500 Strong constraint on modelled global carbon uptake using solar-induced chlorophyll fluorescence data, Sci. Rep., 8, 1–12,
501 https://doi.org/10.1038/s41598-018-20024-w, 2018.

502 O'Dell, C. W., Connor, B., Bösch, H., O'Brien, D., Frankenberg, C., Castano, R., Christi, M., Eldering, D., Fisher, B.,
503 Gunson, M., McDuffie, J., Miller, C. E., Natraj, V., Oyafuso, F., Polonsky, I., Smyth, M., Taylor, T., Toon, G. C., Wennberg,
504 P. O., and Wunch, D.: The ACOS CO2 retrieval algorithm-Part 1: Description and validation against synthetic observations,
505 Atmos. Meas. Tech., 5, 99–121, https://doi.org/10.5194/amt-5-99-2012, 2012.

506 Qiu, R., Han, G., Ma, X., Xu, H., Shi, T., and Zhang, M.: A comparison of OCO-2 SIF, MODIS GPP, and GOSIF data from
507 gross primary production (GPP) estimation and seasonal cycles in North America, Remote Sens., 12,
508 https://doi.org/10.3390/rs12020258, 2020.

509 Reuter, M., Buchwitz, M., Schneising, O., Heymann, J., Bovensmann, H., and Burrows, J. P.: A method for improved
510 SCIAMACHY CO_2 retrieval in the presence of optically thin clouds, Atmos. Meas. Tech., 3, 209–232,
511 https://doi.org/10.5194/amt-3-209-2010, 2010.

512 Sun, K., Liu, X., Nowlan, C. R., Cai, Z., Chance, K., Frankenberg, C., Lee, R. A. M., Pollock, R., Rosenberg, R., and Crisp,
513 D.: Characterization of the OCO-2 instrument line shape functions using on-orbit solar measurements, Atmos. Meas. Tech.,
514 10, 939–953, https://doi.org/10.5194/amt-10-939-2017, 2017b.

515 Sun, Y., Frankenberg, C., Jung, M., Joiner, J., Guanter, L., Köhler, P., and Magney, T.: Overview of Solar-Induced
516 chlorophyll Fluorescence (SIF) from the Orbiting Carbon Observatory-2: Retrieval, cross-mission comparison, and global
517 monitoring for GPP, Remote Sens. Environ., 209, 808–823, https://doi.org/10.1016/j.rse.2018.02.016, 2018.

518 Sun, Y., Frankenberg, C., Wood, J. D., Schimel, D. S., Jung, M., Guanter, L., Drewry, D. T., Verma, M., Porcar-Castell, A.,
519 Griffis, T. J., Gu, L., Magney, T. S., Köhler, P., Evans, B., and Yuen, K.: OCO-2 advances photosynthesis observation from
520 space via solar-induced chlorophyll fluorescence, Science (80-.)., 358, https://doi.org/10.1126/science.aam5747, 2017a.

521   Sun, Y., Fu, R., Dickinson, R., Joiner, J., Frankenberg, C., Gu, L., Xia, Y., and Fernando, N.: Drought onset mechanisms
522   revealed by satellite solar-induced chlorophyll fluorescence: Insights from two contrasting extreme events, J. Geophys. Res.
523   G Biogeosciences, 120, 2427–2440, https://doi.org/10.1002/2015JG003150, 2015.

524   Tramontana, G., Jung, M., Schwalm, C. R., Ichii, K., Camps-Valls, G., Ráduly, B., Reichstein, M., Arain, M. A., Cescatti, A.,
525   Kiely, G., Merbold, L., Serrano-Ortiz, P., Sickert, S., Wolf, S., and Papale, D.: Predicting carbon dioxide and energy fluxes
526   across global FLUXNET sites with regression algorithms, 13, 4291–4313, https://doi.org/10.5194/bg-13-4291-2016, 2016.

527   van der Tol, C., Rossini, M., Cogliati, S., Verhoef, W., Colombo, R., Rascher, U., and Mohammed, G.: A model and
528   measurement comparison of diurnal cycles of sun-induced chlorophyll fluorescence of crops, Remote Sens. Environ., 186,
529   663–677, https://doi.org/10.1016/j.rse.2016.09.021, 2016.

530   Yang, D., Boesch, H., Liu, Y., Somkuti, P., Cai, Z., Chen, X., Di Noia, A., Lin, C., Lu, N., Lyu, D., Parker, R. J., Tian, L.,
531   Wang, M., Webb, A., Yao, L., Yin, Z., Zheng, Y., Deutscher, N. M., Griffith, D. W. T., Hase, F., Kivi, R., Morino, I.,
532   Notholt, J., Ohyama, H., Pollard, D. F., Shiomi, K., Sussmann, R., Té, Y., Velazco, V. A., Warneke, T., and Wunch, D.:
533   Toward High Precision XCO2 Retrievals From TanSat Observations: Retrieval Improvement and Validation Against
534   TCCON Measurements, J. Geophys. Res. Atmos., 125, 1–26, https://doi.org/10.1029/2020JD032794, 2020.

535   Yang, D., Liu, Y., Boesch, H., Yao, L., Di Noia, A., Cai, Z., Lu, N., Lyu, D., Wang, M., Wang, J., Yin, Z., and Zheng, Y.: A
536   New TanSat XCO2 Global Product towards Climate Studies, Adv. Atmos. Sci., 38, 8–11, https://doi.org/10.1007/s00376-
537   020-0297-y, 2021.

538   Yang, D., Liu, Y., Cai, Z., Chen, X., Yao, L., and Lu, D.: First Global Carbon Dioxide Maps Produced from TanSat
539   Measurements, Adv. Atmos. Sci., 35, 621–623, https://doi.org/10.1007/s00376-018-7312-6, 2018.

540   Yang, D., Liu, Y., Cai, Z., Deng, J., Wang, J., and Chen, X.: An advanced carbon dioxide retrieval algorithm for satellite
541   measurements and its application to GOSAT observations, Sci. Bull., 60, 2063–2066, https://doi.org/10.1007/s11434-015-
542   0953-2, 2015b.

543   Yang, X., Tang, J., Mustard, J. F., Lee, J. E., Rossini, M., Joiner, J., Munger, J. W., Kornfeld, A., and Richardson, A. D.:
544   Solar-induced chlorophyll fluorescence that correlates with canopy photosynthesis on diurnal and seasonal scales in a
545   temperate deciduous forest, Geophys. Res. Lett., 42, 2977–2987, https://doi.org/10.1002/2015GL063201, 2015a.

546   Yao, L., Yang, D., Liu, Y., Wang, J., Liu, L., Du, S., Cai, Z., Lu, N., Lyu, D., Wang, M., Yin, Z., and Zheng, Y.: A New
547   Global Solar-induced Chlorophyll Fluorescence (SIF) Data Product from TanSat Measurements, Adv. Atmos. Sci., 38, 341–
548   345, https://doi.org/10.1007/s00376-020-0204-6, 2021.

549   Yin, Y., Byrne, B., Liu, J., Wennberg, P. O., Davis, K. J., Magney, T., Köhler, P., He, L., Jeyaram, R., Humphrey, V.,
550   Gerken, T., Feng, S., Digangi, J. P., and Frankenberg, C.: Cropland Carbon Uptake Delayed and Reduced by 2019 Midwest
551   Floods, AGU Adv., 1, 1–15, https://doi.org/10.1029/2019av000140, 2020.

552   Yoshida, Y., Joiner, J., Tucker, C., Berry, J., Lee, J. E., Walker, G., Reichle, R., Koster, R., Lyapustin, A., and Wang, Y.:
553   The 2010 Russian drought impact on satellite measurements of solar-induced chlorophyll fluorescence: Insights from

554 modeling and comparisons with parameters derived from satellite reflectances, Remote Sens. Environ., 166, 163–177,

555 https://doi.org/10.1016/j.rse.2015.06.008, 2015.

556 Yoshida, Y., Kikuchi, N., Morino, I., Uchino, O., Oshchepkov, S., Bril, A., Saeki, T., Schutgens, N., Toon, G. C., Wunch, D.,

557 Roehl, C. M., Wennberg, P. O., Griffith, D. W. T., Deutscher, N. M., Warneke, T., Notholt, J., Robinson, J., Sherlock, V.,

558 Connor, B., Rettinger, M., Sussmann, R., Ahonen, P., Heikkinen, P., Kyrö, E., Mendonca, J., Strong, K., Hase, F., Dohe, S.,

559 and Yokota, T.: Improvement of the retrieval algorithm for GOSAT SWIR XCO2and XCH4and their validation using

560 TCCON data, Atmos. Meas. Tech., 6, 1533–1547, https://doi.org/10.5194/amt-6-1533-2013, 2013.

561 Yoshida, Y., Ota, Y., Eguchi, N., Kikuchi, N., Nobuta, K., Tran, H., Morino, I., and Yokota, T.: Retrieval algorithm for CO_2

562 and CH_4 column abundances from short-wavelength infrared spectral observations by the Greenhouse gases observing

563 satellite, Atmos. Meas. Tech., 4, 717–734, https://doi.org/10.5194/amt-4-717-2011, 2011.

564 Yu, L., Wen, J., Chang, C. Y., Frankenberg, C., and Sun, Y.: High-Resolution Global Contiguous SIF of OCO-2, Geophys.

565 Res. Lett., 46, 1449–1458, https://doi.org/10.1029/2018GL081109, 2019.

566 Zhang, Y., Guanter, L., Berry, J. A., Joiner, J., van der Tol, C., Huete, A., Gitelson, A., Voigt, M., and Köhler, P.: Estimation

567 of vegetation photosynthetic capacity from space-based measurements of chlorophyll fluorescence for terrestrial biosphere

568 models, Glob. Chang. Biol., 20, 3727–3742, https://doi.org/10.1111/gcb.12664, 2014.

569 Zhang, Y., Xiao, X., Zhang, Y., Wolf, S., Zhou, S., Joiner, J., Guanter, L., Verma, M., Sun, Y., Yang, X., Paul-Limoges, E.,

570 Gough, C. M., Wohlfahrt, G., Gioli, B., van der Tol, C., Yann, N., Lund, M., and de Grandcourt, A.: On the relationship

571 between sub-daily instantaneous and daily total gross primary production: Implications for interpreting satellite-based SIF

572 retrievals, Remote Sens. Environ., 205, 276–289, https://doi.org/10.1016/j.rse.2017.12.009, 2018.

573

574

575

576